

Multiparameter Estimation From Landsat Observations With Topographic Consideration

Hanyu Shi¹, Student Member, IEEE, Zhiqiang Xiao¹, Member, IEEE, Qian Wang¹, and Dongxing Wu

Abstract—The applications of high-spatial-resolution satellite data have been increasing in recent years owing to improvements in sensor techniques, and the errors in estimated parameters induced by ignoring topographic effects are increasingly stressed because their effects are important for parameter retrieval from high-spatial-resolution satellite observations. A coupled surface-atmosphere model is employed to develop a two-step multiparameter estimation scheme to simultaneously estimate multiple parameters (leaf area index, LAI; aerosol optical depth, AOD; photosynthetically active radiation, PAR; incident shortwave radiation, ISR; surface albedo, and fraction of absorbed photosynthetically active radiation, FAPAR) from long-term Landsat 4–8 top-of-atmosphere (TOA) observations. First, the influential parameters of the coupled model are retrieved through optimization retrieval strategies. Then, these estimated parameters are entered into the coupled model to compute the PAR, ISR, surface reflectance, surface albedo, and FAPAR. Validation of this scheme with *in situ* measurements from 57 sites demonstrates that it can successfully estimate multiple parameters from Landsat TOA data, with root mean square errors (RMSEs) of LAI, AOD, FAPAR, visible albedo, shortwave albedo, PAR, and ISR of 0.69, 0.16, 0.13, 0.034, 0.047, 26.80, and 64.28 W/m², respectively. In the two-step multiparameter estimation scheme, atmospheric and topographic corrections of satellite observations are avoided because the atmospheric and topographic effects are incorporated, and the surface anisotropy is also effectively considered. In addition, by using the two-step multiparameter estimation scheme, physical connections among the multiple parameters are ensured since they are estimated from the same physical model.

Index Terms—Consistent estimation, Landsat, radiative transfer, topographic effect.

I. INTRODUCTION

COARSE- and moderate-spatial-resolution remote sensing data, e.g., Clouds and the Earth's Radiant Energy System (CERES), Advanced Very High Resolution Radiometer (AVHRR), and Moderate Resolution Imaging

Spectroradiometer (MODIS) data, have achieved great success in advancing the understanding of the Earth system in recent decades [1], especially in studies of global climate change, water and carbon cycles, vegetation phenology, land cover, and land use change. Concurrently, the needs for high-spatial-resolution data have been growing [2], such as in precision agriculture, forest mapping, ecosystem characterization, and urban studies. According to Zhu *et al.* [3], there have been significant increases in downloads of Landsat data and related publications since 2008, when Landsat data were made publicly available. Furthermore, the recent Sentinel-2 satellites also provide a large number of high-spatial-resolution observations. The increasing applications of high-spatial-resolution data require corresponding algorithms to produce high-spatial-resolution data products. Therefore, developing parameter estimation algorithms for high-spatial-resolution satellite observations and producing high-spatial-resolution data products are important at the current stage.

The topographic effect is an inevitable factor to be considered when processing high-spatial-resolution data. Topography changes the solar-target and target-sensor geometries, affects direct and diffuse solar radiation on land surfaces, and alters the observed radiance [4]. Ignoring topographic effects not only influences the accuracy of forwarding simulation [5]–[8] but also affects the accuracy of estimating parameters [9]–[14]. These surface reflectance models and parameter estimation methods provide ways to eliminate topographic effects, but usually neglect atmospheric effects or assume that the atmospheric parameters are known.

Land surface parameters such as the LAI (leaf area index), surface albedo, and fraction of absorbed photosynthetically active radiation (FAPAR) are traditionally estimated from surface reflectance, the accuracy of which determines the accuracy of the estimated parameters. Atmospheric correction is required to obtain surface reflectance and exact atmospheric parameters are needed; however, retrieving atmospheric parameters requires that surface reflectance is known. Thus, the determination of surface reflectance from atmospheric correction and retrieval of atmospheric parameters are interdependent [15]. Some studies have explored the possibility of 1) directly retrieving surface parameters from top-of-atmosphere (TOA) observations, and 2) jointly retrieving surface and atmospheric parameters. The most classic example of retrieving surface parameters from TOA data is probably estimating the surface albedo from TOA observations, which

Manuscript received December 28, 2020; revised February 1, 2021; accepted February 1, 2021. Date of publication February 17, 2021; date of current version August 30, 2021. This work was supported by the National Natural Science Foundation of China under Grant 41771359. (Corresponding author: Zhiqiang Xiao.)

Hanyu Shi, Zhiqiang Xiao, and Qian Wang are with the State Key Laboratory of Remote Sensing Science, Faculty of Geographical Science, Beijing Normal University, Beijing 100875, China (e-mail: shihanyu@mail.bnu.edu.cn; zhqxiao@bnu.edu.cn; qianwang@bnu.edu.cn).

Dongxing Wu is with the State Key Laboratory of Earth Surface Processes and Resource Ecology, Faculty of Geographical Science, Beijing Normal University, Beijing 100875, China (e-mail: wudongxing@mail.bnu.edu.cn).

Digital Object Identifier 10.1109/TGRS.2021.3057377

1558-0644 © 2021 IEEE. Personal use is permitted, but republication/redistribution requires IEEE permission.
See <https://www.ieee.org/publications/rights/index.html> for more information.

is the basic algorithm of the Global LAnd Surface Satellite (GLASS) surface albedo product [16]. There are also studies that estimate leaf and canopy parameters from TOA data directly [17]–[23]. For the joint estimation of surface and atmospheric parameters, a basic framework for estimating multiple parameters from coupled surface-atmosphere radiative transfer models was developed [15], [24], [25]. For example, in Shi *et al.* [15], the LAI, aerosol optical depth (AOD), FAPAR, surface albedo, and photosynthetically active radiation (PAR) were estimated from MODIS clear-sky observations through an optimized retrieval strategy. Although atmospheric effects were incorporated in these studies, none of them considered the influences of topography on parameter estimation. In addition, the practicability of the joint estimation algorithm has not been tested on high-spatial-resolution data.

The objectives of this study are to retrieve multiple parameters (i.e., LAI, AOD, PAR, FAPAR, incident shortwave radiation (ISR), surface albedo, and reflectance) from 30-meter Landsat TOA observations based on a coupled surface-atmosphere radiative transfer model with topographic effects. A two-step estimation scheme is involved. The influential parameters (LAI and AOD) of the coupled model are first retrieved from the Landsat TOA reflectance and, thereafter, their optimal values are entered into the coupled model to calculate the PAR, FAPAR, reflectance, albedo, and ISR. The coupled model combines atmospheric and topographic effects simultaneously, and these effects are also considered in the multiparameter estimation scheme. Physical consistency among different parameters is also ensured since they are estimated from the same model. This consistency is important to end-users who intend to use remote sensing data products and climate models to study global or regional climate changes [26], [27].

Section II describes the coupled surface-atmosphere model with topographic effects and the two-step multiparameter estimation scheme. The experimental data, including the topographic data, Landsat observations, and field measurement data, are also detailed. Section III illustrates the evaluation of the multiparameter estimation scheme over the selected field sites, and Sections IV and V present a discussion and brief conclusions, respectively.

II. METHODOLOGY AND DATA

In this section, the surface-atmosphere radiative transfer model with topographic effects is introduced and the two-step multiparameter estimation scheme is described. The coupled model is introduced first. Then, a sensitivity analysis of the coupled model is performed to determine the influential parameters of the coupled model, which are retrieved in the later two-step estimation scheme. Finally, evaluation of the estimation scheme is conducted.

A. Coupled Surface-Atmosphere Model With Topographic Consideration

A surface-atmosphere radiative transfer model coupling framework (RTM-CF) with topographic consideration was

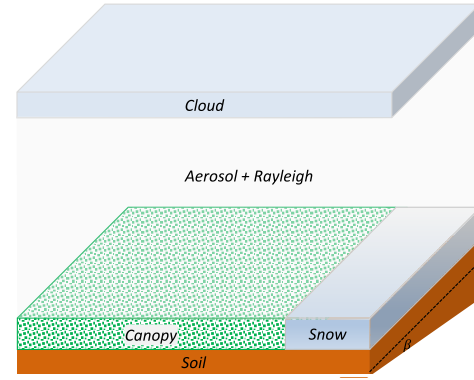


Fig. 1. Coupled surface-atmosphere system over a sloped surface.

developed in [28]. Based on this RTM-CF and the adding-method [29], a multilayer system can be established. Appendix A introduces a necessary background, and details about coupling models can be found in [28] and [29]. The atmospheric, canopy, soil, and snow models are coupled to simulate TOA reflectance. Fig. 1 shows the schematic of the multilayer system. The inclined land indicates the underlying surface associated with the slope (0° – 90°) and aspect (0° – 360°).

1) *Atmospheric Part:* For the atmospheric layers, atmospheric variables are derived from the atmospheric radiative transfer model in libRadtran [30]. The retrieval algorithm for MODIS cloud parameters is used as a reference, and it models clouds as a superposition layer [31]. libRadtran is a widely used atmospheric transfer model and has been applied in various studies, such as those involving remotely sensed clouds, aerosols, and trace gases in the Earth’s atmosphere [30]. libRadtran is adopted to generate official MODIS and Visible Infrared Imaging Radiometer Suite (VIIRS) cloud parameter products [31] and is used by the Sentinel team to conduct atmospheric correction on Sentinel-2 observations [32]. Water and ice clouds are considered separately owing to their different optical properties. Two cloud parameters, cloud effective radius (CER) and cloud water content (CWC), are involved if the cloud location is predefined.

We define the aerosol and Rayleigh layer with variable matrices R_t^a , R_b^a , T_d^a , and T_u^a , where the superscript “a”; indicates the atmosphere without clouds (physical explanations of the variables in this section is given in Appendix A). Similarly, the cloud layer is defined with R_t^c , R_b^c , T_d^c , and T_u^c , where the superscript “c” represents clouds. The whole atmospheric layer (the superscript “A” indicates the atmosphere) has optical variable matrices [29], [33]

$$R_t^A = R_t^c + T_u^c (I - R_t^a R_b^c)^{-1} R_t^a T_d^c \quad (1a)$$

$$R_b^A = R_b^a + T_d^a (I - R_b^c R_t^a)^{-1} R_b^c T_u^a \quad (1b)$$

$$T_d^A = T_d^a (I - R_b^c R_t^a)^{-1} T_d^c \quad (1c)$$

$$T_u^A = T_u^c (I - R_t^a R_b^c)^{-1} T_u^a. \quad (1d)$$

To accelerate the calculations, the look up tables (LUTs) of R_t^a , R_b^a , T_u^a , and T_d^a are precalculated. To reduce the LUT

TABLE I
PARAMETERS FOR THE COUPLED MODEL

| Type | Parameter | Symbol | Values | Units |
|------------|-------------------------------------|-------------|----------------------|-------------------------|
| Geometry | Solar zenith angle | θ_s | 0–85 | degrees |
| | Solar azimuth angle | φ_s | 0–360 | degrees |
| | View zenith angle | θ_v | 0–85 | degrees |
| | View azimuth angle | φ_v | 0–360 | degrees |
| | Elevation | elv | 0–8 | km |
| | Slope | β | 0–90 | degrees |
| | Aspect | φ_T | 0–360 | degrees |
| | Sky view factor | V_{sky} | 0–1 | – |
| Atmosphere | Cloud type | – | Water/Ice | – |
| | Cloud effective radius | CER | 1–60 | μm |
| | Cloud water content | CWC | 0–4 | g/m^3 |
| | Aerosol optical depth at 550 nm | AOD | 0–2 | – |
| Vegetation | Leaf area index | LAI | 0–8 | m^2/m^2 |
| | Hot-spot parameter | sl | 0.1 | – |
| | Foliage clumping parameter | clmp | 0.4–1.2 | – |
| | Displacement parameter | szz | 1.2 | – |
| | Elliptical leaf angle distribution | eln | 2.0 | – |
| | Modal leaf angle | thm | 75.0 | degrees |
| | Refraction index factor | nratio | 0.9 | – |
| | Leaf specific weight | SLW | 40–200 | g/m^2 |
| | Leaf water content | c1 | 80–180 | % of SLW |
| | Chlorophyll AB content | c2 | 0.2–0.7 | % of SLW |
| | Leaf dry matter content | c3 | 98 | % of SLW |
| | Anthocyanin | c4 | 0.038 | % of SLW |
| | Leaf structure parameter | N | 1.624 | – |
| Soil | Weight of the first Price function | s1 | 0.05–0.9 | – |
| | Weight of the second Price function | s2 | -0.05 | – |
| | Weight of the third Price function | s3 | 0.0 | – |
| | Weight of the fourth Price function | s4 | 0.0 | – |
| Snow | Effective diameter of grains | d | 1–5 | mm |
| | pollutants concentration | M | 4.5×10^{-8} | – |
| | Weighting factor | ω | 0–1 | – |

size and simplify the model, the default aerosol model is used. The clear-sky atmospheric variables are presimulated at various solar zenith angles, view zenith angles, relative azimuth angles, elevations, and 550 nm AODs. Similarly, the cloud optical variables in (1) are presimulated at various solar zenith angles, view zenith angles, relative azimuth angles, CWCs, and CERs. The settings for generating LUTs of these atmospheric variables are given in Table II.

2) *Surface Part*: According to Shi *et al.* [24], the reflectance matrix for the underlying land surface R_s^L (the superscript “L” indicates land) is modeled as

$$R_s^L = (1 - \omega)R_s^v + \omega R_s^i \quad (2)$$

where R_s^i is the reflectance matrix of snow, which is determined from the asymptotic radiative transfer (ART) model [34]. The two main parameters used by the ART

model are the diameter of snow grains (d) and the pollutant proportion (M). The imaginary part of the ice refractive index is also needed to drive the ART model, and its values are from [35]. The ART model is highly efficient and has been widely used for the simulation of snow reflectance. Evaluation by field measurements and satellite data sets demonstrate that the ART model has a high accuracy for view zenith angles less than 60° [34], [36]. R_s^v is the snow-free reflectance matrix above the canopy

$$R_s^v = R_t^v + T_u^v (I - R_s^s R_b^v)^{-1} R_s^s T_d^v \quad (3)$$

where the superscript “v” indicates vegetation. The reflectance matrices of the canopy, R_t^v and R_b^v , and the transmittance matrices, T_u^v and T_d^v , are simulated by the A two-lay Canopy Reflectance Model (ACRM). The ACRM is an extension of the homogeneous multispectral canopy reflectance model [37]

TABLE II
SETTINGS FOR GENERATING LOOK-UP-TABLES OF ATMOSPHERIC VARIABLES

| | |
|--------------------------------|---|
| Solar zenith angle | 0°–85° (5° spacing) |
| View zenith angle | 0°–70° (5° spacing) |
| Relative azimuth angle | 0°–70° (5° spacing) |
| Elevations | 0–8 km (0.5 km spacing) |
| Aerosol optical depth (550 nm) | 0.001, 0.01, 0.02, 0.03, 0.05, 0.07, 0.1, 0.15, 0.2, 0.25, 0.3, 0.4, 0.5, 0.6, 0.7, 0.8, 0.9, 1.0, 2.0 |
| Cloud type | Water cloud; Ice cloud |
| Cloud water content | 0.0001, 0.0003, 0.0005, 0.0007, 0.001, 0.003, 0.005, 0.007, 0.01, 0.015, 0.02, 0.025, 0.03, 0.04, 0.05, 0.06, 0.08, 0.1, 0.15, 0.2, 0.25, 0.4, 0.6, 0.8, 1.0, 2.0, 4.0 g/m ³ |
| Cloud effective radius | water clouds: 1, 2, 3, 4, 5, 6, 7, 8, 9, 10, 11, 12, 14, 16, 18, 20, 22, 24, 25 μm ice clouds: 5–60 μm (5 μm spacing) |

and the Markov chain canopy reflectance model [38]. The ACRM is a homogeneous turbid model that accounts for hot-spot effects, specular reflection of direct irradiance on leaves, and the elliptical leaf angle distribution (LAD) [39]. The PROSPECT (version 3) leaf optical model is used by the ACRM to calculate leaf reflectance and transmittance, and the pigment absorption spectra from PROSPECT-D [40] is used in this study to replace the default ones [41]. In ACRM, the SLW (specific leaf weight) parameter (see Table I) is introduced as a normalized factor, and the biochemical parameters are expressed as its fraction [41]. Thus, the actual leaf pigment contents are equal to the products of SLW and their input values. R_s^s is the reflectance matrix of soil, calculated from the Walthall-Price model, and the superscript “s” represents soil. The Walthall model is an empirical soil reflectance model that accounts for non-Lambertian characters [42], [43]. A soil spectrum is required to be input into the Walthall model, and the spectrum developed by Price [44] is adopted. Through the singular value decomposition method, the variety of soil spectra is described by only four basic functions, so the number of soil parameters is reduced [44]. The Walthall-Price model is also the default soil model in the ACRM. The parameter ω in (2) is a weighting factor, which is 0 for snow-free conditions.

3) *TOA Reflectance Modeling*: By considering a terrain surface with a slope of β and an aspect of φ_T , the TOA bidirectional reflectance over sloping surfaces is modeled as

$$\begin{aligned}
 r_{so}^A &= \rho_{so}^A + \tau_{oo}^A r_{so}^L F_{sun} \tau_{ss}^A \\
 &+ \frac{\tau_{do}^A V_{sky} (r_{sd}^L F_{sun} \tau_{ss}^A + r_{dd}^L F_{sky} \tau_{sd}^A)}{1 - r_{dd}^L \rho_{dd}^{A,b}} \\
 &+ \frac{\tau_{oo}^A r_{do}^L (F_{sky} \tau_{sd}^A + \rho_{dd}^{A,b} r_{sd}^L F_{sun} \tau_{ss}^A)}{1 - r_{dd}^L \rho_{dd}^{A,b}} \quad (4)
 \end{aligned}$$

and F_{sun} and F_{sky} [4] are

$$F_{sun} = \zeta \frac{\cos \theta_{is}}{\cos \theta_s}; \quad F_{sky} = \tau_{ss}^A \frac{\cos \theta_{is}}{\cos \theta_s} + (1 - \tau_{ss}^A) V_{sky} \quad (5)$$

where θ_s and φ_s are the solar zenith and azimuth angles, respectively. Further, $\cos \theta_{is} = \cos \theta_s \cos \beta +$

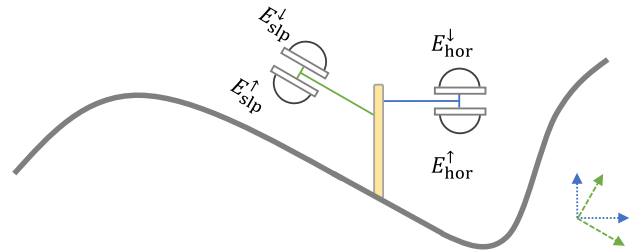


Fig. 2. Schematic for surface radiation fluxes that refers to the sloping (in green) and horizontal (in blue) planes. The slope-parallel positioned radiometers measure surface radiation fluxes (E_{slip}^{\downarrow} and E_{slip}^{\uparrow}) that refer to the sloping surface, and the horizontal radiometers measure surface radiation fluxes (E_{hor}^{\downarrow} and E_{hor}^{\uparrow}) that refer to the horizontal plane. Proximal radiometers are usually installed horizontally in the field.

$\sin \theta_s \sin \beta \cos(\varphi_s - \varphi_T)$, where ζ is a binary factor (0 or 1) that indicates whether the pixel is self-shadowed or shielded by other pixels [45], [46]. θ_{is} is the intrinsic solar zenith angle, which refers to the slope surface. V_{sky} is the sky view factor, which can be precalculated from digital elevation model (DEM) data for a specific number of azimuth directions [46]. This terrain algorithm considers the topographic effects on direct solar radiation and the obstruction of the surrounding topography for hemispherical radiation.

The input parameters of the TOA reflectance model are given in Table I, and the detailed modeling process can be found in [28].

4) *Modeling of the Surface Parameters*: As shown in Fig. 2, surface radiation fluxes are different when taking different reference planes (the horizontal plane and the slope-parallel plane). E_{slip}^{\downarrow} and E_{slip}^{\uparrow} represent downward and upward radiation that refer to the sloping surface, respectively; and E_{hor}^{\downarrow} and E_{hor}^{\uparrow} are downward and upward radiation that refer to the horizontal plane, respectively. Detailed modeling processes of these parameters and differences between sloping- and horizontal-referenced parameters can be found in [28] and are not repeated.

PAR and ISR are the total incident surface solar radiation (SSR) in the spectral ranges of 400–700 nm and

300–3000 nm, respectively. The SSR on the slope is given as

$$\text{SSR}_{\text{sip}} = \int_{\lambda_1}^{\lambda_2} P_1 (I - R_b^A R_s^L)^{-1} P_T^{\text{in}} T_d^A E_d^A d\lambda \quad (6)$$

and the corresponding SSR on the horizontal plane is

$$\text{SSR}_{\text{hor}} = \int_{\lambda_1}^{\lambda_2} P_1 H_T (I - R_b^A R_s^L)^{-1} P_T^{\text{in}} T_d^A E_d^A d\lambda \quad (7)$$

where

$$H_T = \begin{bmatrix} H_{\text{sun}} & 0 \\ 0 & V_{\text{sky}} \end{bmatrix}; H_{\text{sun}} = \zeta \frac{\cos \theta_s}{\cos \theta_{\text{is}}} \quad (8)$$

and $E_d^A = [E_s^A \cos(\theta_s), 0]^T$ is the TOA solar irradiance matrix and E_s^A is the monochromatic extra-terrestrial solar irradiance on the plane that is perpendicular to the solar beam. $P_1 = [1, 1]$ is an extraction matrix. λ_1 and λ_2 are 400 and 700 nm, respectively, for PAR, whereas they are 300 and 3000 nm for ISR.

The surface albedo is the ratio of the reflected and incident radiation, and its equation refers to the slope coordinate as follows:

$$\text{Albedo}_{\text{sip}} = \frac{\int_{\lambda_1}^{\lambda_2} P_2 R_s^L (I - R_b^A R_s^L)^{-1} P_T^{\text{in}} T_d^A E_d^A d\lambda}{\int_{\lambda_1}^{\lambda_2} P_1 (I - R_b^A R_s^L)^{-1} P_T^{\text{in}} T_d^A E_d^A d\lambda} \quad (9)$$

and its equation for the horizontal plane is given as

$$\text{Albedo}_{\text{hor}} = \frac{\int_{\lambda_1}^{\lambda_2} P_2 P_T^{\text{out}} R_s^L (I - R_b^A R_s^L)^{-1} P_T^{\text{in}} T_d^A E_d^A d\lambda}{\int_{\lambda_1}^{\lambda_2} P_1 H_T (I - R_b^A R_s^L)^{-1} P_T^{\text{in}} T_d^A E_d^A d\lambda} \quad (10)$$

where $P_2 = [1, 0]$. For the visible albedo, λ_1 and λ_2 are 400 and 700 nm, respectively, whereas they are 300 and 3000 nm for the shortwave albedo.

Absorbed photosynthesis active radiation (APAR) is the portion of PAR absorbed by vegetation, and FAPAR is their ratio, i.e., $\text{FAPAR} = \text{APAR}/\text{PAR}$

$$\text{APAR} = (1 - \omega) \cdot \int_{400}^{700} [(P_1 - P_2 R_s^L)(P_1 - P_2 R_s^s) \tilde{D}^v] (I - R_b^A R_s^L)^{-1} P_T^{\text{in}} T_d^A E_d^A d\lambda \quad (11)$$

where $\tilde{D}^v = (I - R_b^v R_s^s)^{-1} T_d^v$ is the equivalent transmittance matrix for the canopy [24]. ω is 0 for a snow-free land surface. It is critical that FAPAR value will be different if different coordinates (PAR_{sip} or PAR_{hor}) are taken as a reference. The value $\text{FAPAR} = \text{APAR}/\text{PAR}_{\text{sip}}$ is used in this study.

The surface reflectances of the Landsat channels are output, and they are also different with different coordinates

$$\text{BRF}_{\text{hor}} = \text{BRF}_{\text{sip}} \cdot F_{\text{sun}}. \quad (12)$$

In this study, if not specified, the downwelling radiation (PAR and ISR) and albedo parameters referenced to the horizontal coordinate are compared with the field-measured data because the proximal sensors are set horizontally in the field for the selected sites.

B. Global Sensitivity Analysis

The extension of the Fourier amplitude sensitivity testing (EFAST) method is adopted to identify influential parameters of the coupled surface-atmosphere model. EFAST is a global sensitivity analysis method, which means it provides information on how the variation of model output is produced by the variation of model input parameters individually and globally through interactions with each other [15], [22], [47]. EFAST is applied to (4) since TOA reflectance is used in retrieval. EFAST is a variance-based method, and it decomposes the variance in the output into fractions that can be attributed to the input parameters [48]. Variance-based methods have been widely used in the remote sensing community [22], [49]–[51]. The geometric solar, view, and terrain angles are not included in the sensitivity analysis because they are given variables, and it is not necessary to test their retrievability [51]. Ideally, a sensitivity analysis should be conducted over all possible geometric angles. However, this is a massive task, and a previous study [49], as well as our experience, showed that the influential parameters are generally the same under different geometric angles.

Therefore, the observation and terrain geometries are fixed. The view zenith angle is set to 0° , considering that Landsat observations have small zenith angles. Two solar zenith angles (30° and 50°) over a flat and a sloping surface ($\beta = 30^\circ$) were tested independently under clear atmospheric and snow-free conditions. The results under different geometric conditions are similar, although the absolute values have discrepancies. Four influential parameters are identified at the shortwave bands of Landsat, viz. AOD, LAI, SLW, and s1. The four parameters are treated as free variables during retrieval under clear atmospheric and snow-free surface conditions. Under clear atmospheric and snow-covered surface conditions, snow contributes the most to the observations due to its high reflectance. Thus, two snow parameters (the effective diameter of snow grains, d , and the snow weighting factor, ω) are identified as influential and are set as free variables. Under cloudy atmospheric conditions, the two cloud parameters (CER and CWC) are identified as influential parameters. The sensitivity analysis results for clear atmospheric and snow-free conditions ($\theta_s = 30^\circ$ and $\beta = 0^\circ$) are illustrated in Fig. 3, and the other results are not shown here.

C. Two-Step Estimation Scheme Considering Topography

The multiparameter estimation scheme is a two-step process. The first step is the direct estimation part. The influential parameters of the coupled model are retrieved from Landsat TOA observations based on an optimization inversion strategy. The second step is the indirect estimation part. The retrieved optimal parameters are entered into the coupled model to calculate the PAR, ISR, surface reflectance, surface albedo, and FAPAR.

Identifications of the atmospheric (clear or cloudy) and surface (snow covered or not) states is required, and this information comes from the Landsat data set. If a pixel is identified as clear and snow-free, then no cloud and snow

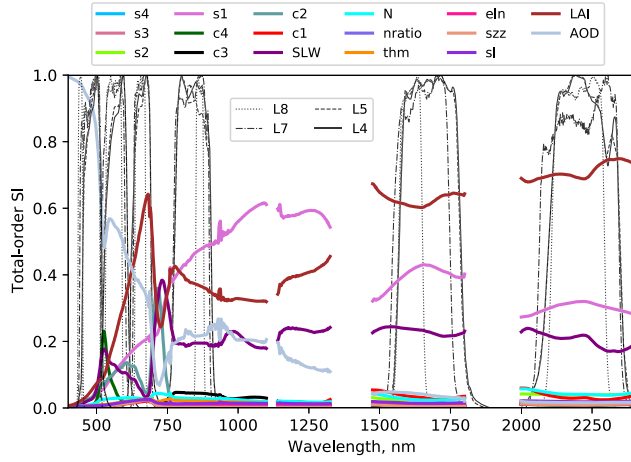


Fig. 3. Total-order sensitivity index (SI) of the input parameters of the coupled model. The relative spectral response of Landsat 4 (L4), 5 (L5), 7 (L7), and 8 (L8) are overlaid. Strong absorption regions (1100–1400, 1325–1475, and 1800–2000 nm) are masked. For interpretation of the references to color in this figure legend, the reader is referred to the web version of this article.

parameters are involved. The merit function is given as

$$J(\mathbf{m}) = \frac{1}{2} [(\mathbf{g}(\mathbf{m}) - \mathbf{y}_o)^T \mathbf{C}_D^{-1} (\mathbf{g}(\mathbf{m}) - \mathbf{y}_o) + (\mathbf{m} - \mathbf{m}_p)^T \mathbf{C}_M^{-1} (\mathbf{m} - \mathbf{m}_p)] \quad (13)$$

where \mathbf{m} is the vector that includes the parameters to be estimated, $\mathbf{m} = [\text{AOD}, \text{LAI}, \text{SLW}, \text{s1}]^T$, and \mathbf{m}_p is the prior estimation of \mathbf{m} . In this study, the GLASS LAI climatology and MERRA-2 AOD data sets provided the prior values of LAI and AOD, respectively. Further details are given in Section II-D2. The Landsat TOA reflectance is included in $\mathbf{y}_o = [b_1, b_2, b_3, b_4, b_5, b_6, b_7]^T$ (b_i , $i = 1, \dots, 7$ is the i -th band TOA reflectance of Landsat; b_6 is for Landsat 8 only), and it includes the influences of topography. $\mathbf{g}(\mathbf{m})$ is the modeled Landsat TOA observations, and the proposed TOA reflectance model with topographic effects (4) is used. \mathbf{C}_M is the covariance matrix for errors in the prior information, and \mathbf{C}_D is the covariance matrix describing the observational uncertainties. The uncertainties in the prior values and Landsat TOA reflectance are assumed to be uncorrelated. Thus, \mathbf{C}_M and \mathbf{C}_D are diagonal [52]. Landsat TOA reflectance does not provide uncertainty values. In this study, the six or seven diagonal elements of \mathbf{C}_D are set to 0.04 times the corresponding reflectance values. The first and second diagonal elements of \mathbf{C}_M are $0.05 \times \text{AOD}$ and the standard deviation of the 18-year GLASS LAI, respectively, as discussed in Section II-D2. The uncertainty values for SLW and s1 are 30.0 and 0.07, respectively, which are identical to the settings in the study by [15] and are described in [41].

If a pixel is identified as a clear and snow pixel, only the effective diameter of snow grains (d) and the snow weighting factor (ω) are involved. The pollutant concentration is fixed because it has much less influence than d , as found by EFAST sensitivity analysis (the results are not shown). The merit function is given as

$$J(\mathbf{m}) = \frac{1}{2} [(\mathbf{g}(\mathbf{m}) - \mathbf{y}_o)^T \mathbf{C}_D^{-1} (\mathbf{g}(\mathbf{m}) - \mathbf{y}_o)] \quad (14)$$

where $\mathbf{m} = [\omega, d]^T$. The atmosphere, canopy, and soil parameters are fixed under this condition. Particularly, prior LAI and AOD values are used as inputs.

If a pixel is identified as cloudy, then the surface parameters are fixed, and only the two cloud parameters CER and CWC are free variables. The merit function has the same form as (14), but $\mathbf{m} = [\text{CER}, \text{CWC}]^T$. Owing to the lack of cloud type identification, the retrieval is conducted for both water and ice cloud types, and retrieval with a smaller $J(\mathbf{m})$ value is selected.

For all the retrievals, the shuffled complex evolution (SCE) algorithm [53] was used in this study to search for the optimal estimates of the variables. SCE is a global optimization strategy. It does not rely on derivatives of the target merit function and has been proven flexible and robust [54]. The advantages of simple production with the concepts of controlled random search, competitive evolution, and the complex shuffling strategy are combined in SCE [55]. Besides, it is less sensitive to initial values [53].

The direct estimation part is finished once the optimal values of the influential parameters are retrieved. The retrieved optimal values are then input into the coupled model to calculate the PAR, ISR, surface reflectance, albedo, and FAPAR, and the estimation process is finished.

D. Data

1) *Landsat Observation*: Shortwave Landsat 4, 5, 7, and 8 data are used in this study. They have a spatial resolution of approximately 30 m. Landsat 4–7 have similar spectral responses, while Landsat 8 has an extra blue band, as shown in Fig. 3. The quality control (QC) information included in the Landsat data provides the identification of the cloud and snow states for each pixel [56], which is used for retrieval. The Landsat Level-1 TOA reflectance is used to estimate multiple parameters, while the Level-2 surface reflectance data product is used for comparisons with the retrieved surface reflectance values.

2) *Auxiliary Data*: The Advanced Spaceborne Thermal Emission and Reflection Radiometer (ASTER) Global Digital Elevation Model (ASTGTM) global 1-arc-second data set provides elevation values [57], which are further used to calculate the slope, aspect, and sky view factor [45], [46], [58].

Prior information on the LAI, AOD, and clumping index (CI) is used in this study. A global LAI climatology map generated from the 18-year (2001–2018) GLASS LAI product [59] is used. The averaged values and standard deviations are used as the prior and its uncertainty in the retrieval, respectively. The MERRA-2 AOD product [60] provides prior AOD values. The evaluations of the MERRA-2 AOD product [61], [62] indicated its high accuracy, and the uncertainty value of $0.05 \times \text{AOD}$ is used in the retrieval process. The global CI product produced by [63] is used for the CI. This 18-year (2001–2018) CI product was processed to generate a global climatology CI map, which is the input in the retrieval process.

3) *Field Data*: Existing data sets with field measurements used were collected to evaluate the retrieval results. All seven

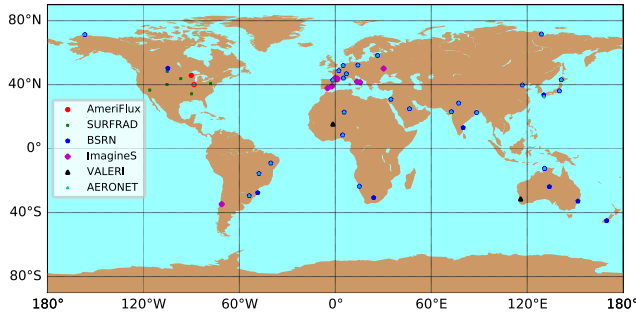


Fig. 4. Field sites used for validation in this study. Different field networks/projects are illustrated with different symbols. For interpretation of the references to color in this figure legend, the reader is referred to the web version of this article.

sites of the Surface Radiation (SURFRAD) project are used to validate the PAR, ISR, shortwave albedo, and AOD. The measurements from the SURFRAD sites have a temporal resolution of 1 or 3 min, and only the data that are labeled good quality are used. All the Landsat 4–8 observations (1980–2018) at the seven sites were downloaded, and multiple parameter estimations were conducted and evaluated.

The field LAI and FAPAR were primarily obtained from the ImagineS database (<http://fp7-imagines.eu/>) and the Validation of Land European Remote sensing Instruments (VALERI) database (<http://w3.avignon.inra.fr/valeri/>). The selected sites provide high-spatial-resolution LAI/FAPAR maps derived from *in situ* point measures and Landsat data. The corresponding Landsat TOA observations at the *in situ* pixels are collected and retrieved for comparison with the reference values.

The baseline surface radiation network (BSRN) database provides long-term shortwave radiation data from globally distributed sites [64], and 33 such sites are used in this study. The BSRN provides a toolbox [65] to provide QC information for the data, and only good-quality data are used. Two sites from the AmeriFlux project are selected, both of which provide field-measured visible albedo values, and the US-Bo1 site also has field LAI measurements. The AOD data from the AERONET site near the selected BSRN and AmeriFlux sites are used based on availability. The quality-assured Version 3 and Level 2.0 AOD values in 15-min intervals are extracted [66].

The geolocations of the selected field sites are shown in Fig. 4, and the corresponding information is listed in Table III.

4) *Simulated Data*: Most of the long-term flux measurement sites are set on areas as flat as possible for easy maintenance. As seen from Table III, the majority of the slope values of the field sites (57 in total) are less than 6°. Therefore, the influence of topography on estimating parameters cannot be well illustrated through *in situ* data only. A simulation experiment is conducted to demonstrate the importance of topographic effects on estimating parameters by using the simulated TOA reflectance. Then, multiple parameters are retrieved from the simulated reflectance but using the model that does not consider topographic effects. The differences between the estimated parameters and the “true” values are caused by ignoring the topographic effects. Without

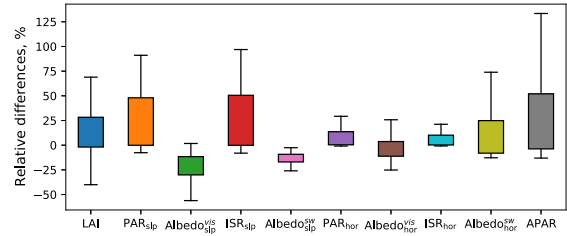


Fig. 5. Relative errors for the estimated parameters when ignoring the influences of topography. Refer Section II for the definitions of the parameters. For interpretation of the references to color in this figure legend, the reader is referred to the web version of this article.

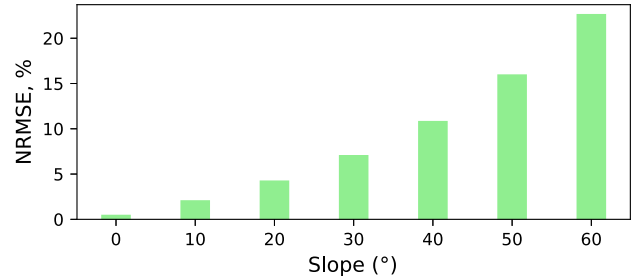


Fig. 6. Influences of slope values on the estimation of the multiple parameters. The normalized NRMSE values are calculated for all retrieved parameters, and are then grouped by slope values. $NRMSE = RMSE / (Max - Min)$.

a loss of generality, the sensor is assumed to be nadir-viewing, and the solar zenith angle is fixed to 25°. Three LAI values (1, 3, and 5) and two soil reflectance spectra (high reflective and low reflective) are used. The slope values are simulated from 0°–60° with an interval of 10°, and the aspect values are simulated from 0°–180° with an interval of 45°.

III. RESULTS AND ANALYSES

A. Simulated Data

The importance of topographic effects on parameter estimation is demonstrated by using simulated data (refer to Section II-D4) first before applying the estimation algorithm to the Landsat observations. The simulated TOA reflectance over different surface conditions is used in the retrieval, and the model without the consideration of topography is applied. Fig. 5 shows the boxplot of the relative differences for different parameters, each of which is the statistical result over all simulated data. It can be seen that ignoring topographic effects can induce an error of 50% for LAI, and the errors in the other ten radiation-related parameters are also significant. The errors induced by neglecting topographic effects that grouped by slope values are plotted in Fig. 6. The normalized root mean square error (NRMSE) values are calculated for every retrieved parameter and are then grouped by slope values. The metric NRMSE, which is calculated by root mean square error (RMSE)/(Max–Min), is used to remove the amplitude of different parameters. Fig. 6 shows that NRMSE increases with slope values, which is consistent with the estimation errors increasing with slope values if ignoring topographic effects.

TABLE III
 INFORMATION OF THE 57 SELECTED FIELD SITES FOR THE VALIDATION OF ESTIMATED PARAMETERS. THE SURFACE
 TYPE IS FROM THE DESCRIPTIONS OF THE SITE, AND A N/A SYMBOL IS FILLED IF NOT PROVIDED

| Latitude (°) | Longitude (°) | Site name | Project | Elevation (m) | Slope (°) | Aspect (°) | Sky view factor | Surface type |
|--------------|---------------|-------------|-------------------|---------------|-----------|------------|-----------------|----------------|
| 40.006 | -88.290 | US-Bo1 | AmeriFlux/AERONET | 213 | 1.20 | 345.46 | 0.9934 | Crop |
| 45.806 | -90.080 | US-WCr | AmeriFlux | 524 | 3.72 | 79.16 | 0.9823 | Forest |
| 34.255 | -89.873 | GWN | SURFRAD | 92 | 4.57 | 78.25 | 0.9942 | Grass |
| 40.052 | -88.373 | BND | SURFRAD | 202 | 4.10 | 286.51 | 0.9910 | Crop |
| 40.125 | -105.237 | TBL | SURFRAD | 1688 | 5.07 | 303.42 | 0.9945 | Grass |
| 43.734 | -96.623 | SXF | SURFRAD | 476 | 4.47 | 248.61 | 0.9917 | Grass |
| 36.624 | -116.019 | DRA | SURFRAD | 998 | 5.09 | 196.42 | 0.9905 | Desert, rock |
| 48.308 | -105.102 | FPK | SURFRAD | 637 | 4.57 | 81.22 | 0.9963 | Grass |
| 40.720 | -77.931 | PSU | SURFRAD | 372 | 3.19 | 59.31 | 0.9973 | Crop |
| 22.790 | 5.529 | TAM | BSRN/AERONET | 1371 | 1.06 | 331.69 | 0.9969 | Desert, rock |
| 8.533 | 4.567 | ILO | BSRN/AERONET | 258 | 7.25 | 95.50 | 0.9938 | Shrub |
| -23.561 | 15.042 | GOB | BSRN/AERONET | 415 | 2.86 | 255.87 | 0.9984 | Desert gravel |
| -30.667 | 23.993 | DAA | BSRN | 1267 | 3.76 | 90.00 | 0.9913 | Sand |
| 30.860 | 34.779 | SBO | BSRN/AERONET | 463 | 2.44 | 95.48 | 0.9970 | Desert, rock |
| 24.910 | 46.410 | SOV | BSRN/AERONET | 764 | 12.48 | 64.98 | 0.9872 | Desert, sand |
| 23.110 | 72.628 | GAN | BSRN/AERONET | 62 | 2.79 | 54.24 | 0.9977 | N/A |
| 28.425 | 77.156 | GUR | BSRN/AERONET | 263 | 1.06 | 311.52 | 0.9997 | N/A |
| 13.092 | 79.974 | TIR | BSRN | 27 | 3.45 | 331.23 | 0.9946 | N/A |
| 22.554 | 88.306 | HOW | BSRN/AERONET | 10 | 4.76 | 267.20 | 0.9954 | N/A |
| 39.754 | 116.962 | XIA | BSRN/AERONET | 21 | 5.15 | 68.84 | 0.9979 | Desert, rock |
| 43.060 | 141.329 | SAP | BSRN/AERONET | 23 | 3.51 | 174.82 | 0.9955 | Asphalt |
| 36.058 | 140.126 | TAT | BSRN/AERONET | 27 | 5.52 | 50.86 | 0.9937 | Grass |
| 33.582 | 130.376 | FUA | BSRN/AERONET | 6 | 0.75 | 21.67 | 0.9992 | Asphalt |
| -12.425 | 130.891 | DAR | BSRN/AERONET | 37 | 5.75 | 338.30 | 0.9972 | Grass |
| -12.424 | 130.893 | DWN | BSRN/AERONET | 28 | 2.62 | 95.11 | 0.9971 | Grass |
| -23.798 | 133.888 | ASP | BSRN | 540 | 1.65 | 171.18 | 0.9997 | Grass |
| -32.884 | 151.729 | NEW | BSRN | 10 | 2.25 | 21.52 | 0.9989 | N/A |
| -45.045 | 169.689 | LAU | BSRN | 332 | 2.57 | 296.93 | 0.9905 | Grass |
| 42.816 | -1.601 | CNR | BSRN/AERONET | 441 | 4.16 | 80.33 | 0.9886 | Asphalt |
| 44.083 | 5.059 | CAR | BSRN/AERONET | 98 | 2.42 | 164.54 | 0.9985 | Cultivated |
| 46.815 | 6.944 | PAY | BSRN/AERONET | 492 | 3.45 | 118.19 | 0.9981 | Cultivated |
| 48.713 | 2.208 | PAL | BSRN/AERONET | 154 | 6.58 | 324.25 | 0.9887 | Concrete |
| 51.971 | 4.927 | CAB | BSRN/AERONET | 15 | 1.89 | 277.07 | 0.9994 | Grass |
| 52.210 | 14.122 | LIN | BSRN/AERONET | 111 | 9.73 | 355.59 | 0.9887 | Cultivated |
| 58.254 | 26.462 | TOR | BSRN/AERONET | 27 | 3.73 | 339.31 | 0.9640 | Grass |
| 71.586 | 128.919 | TIK | BSRN/AERONET | 54 | 5.32 | 195.95 | 0.9682 | Tundra |
| 71.323 | -156.607 | BAR | BSRN/AERONET | 22 | 0.00 | - | 0.9998 | Tundra |
| 50.205 | -104.713 | REG | BSRN | 592 | 2.36 | 217.81 | 0.9920 | Cultivated |
| -9.068 | -40.319 | PTR | BSRN/AERONET | 380 | 8.32 | 125.75 | 0.9946 | Concrete |
| -15.601 | -47.713 | BRB | BSRN/AERONET | 994 | 2.66 | 15.71 | 0.9974 | Concrete |
| -29.443 | -53.823 | SMS | BSRN/AERONET | 482 | 2.11 | 352.78 | 0.9989 | Concrete/Grass |
| -27.605 | -48.523 | FLO | BSRN | 21 | 5.95 | 20.49 | 0.9940 | Concrete |
| 41.464 | 15.487 | Capitanata | ImagineS | - | - | - | - | Crop |
| 50.077 | 30.232 | Pshenichne | ImagineS | - | - | - | - | Maize |
| 41.850 | 13.590 | Collelongo | ImagineS | - | - | - | - | Forest |
| 39.054 | -2.101 | Barrax | ImagineS | - | - | - | - | Crop |
| -34.723 | -71.002 | SanFernando | ImagineS | - | - | - | - | Crop |
| 37.824 | -4.869 | LaReina | ImagineS | - | - | - | - | Crop |
| 43.974 | 0.336 | AHSPECT-CON | ImagineS | - | - | - | - | Crop |
| 43.994 | -0.047 | AHSPECT-CRE | ImagineS | - | - | - | - | Crop |
| 43.666 | 0.220 | AHSPECT-PEY | ImagineS | - | - | - | - | Crop |
| 43.824 | 1.175 | AHSPECT-SAV | ImagineS | - | - | - | - | Crop |
| 43.640 | -0.434 | AHSPECT-URG | ImagineS | - | - | - | - | Crop |
| 43.504 | 1.171 | SouthWest | ImagineS | - | - | - | - | Crop |
| 15.331 | -1.475 | Hombori | VALERI | - | - | - | - | Grass |
| -31.534 | 115.882 | Gnangara | VALERI | - | - | - | - | Shrub |

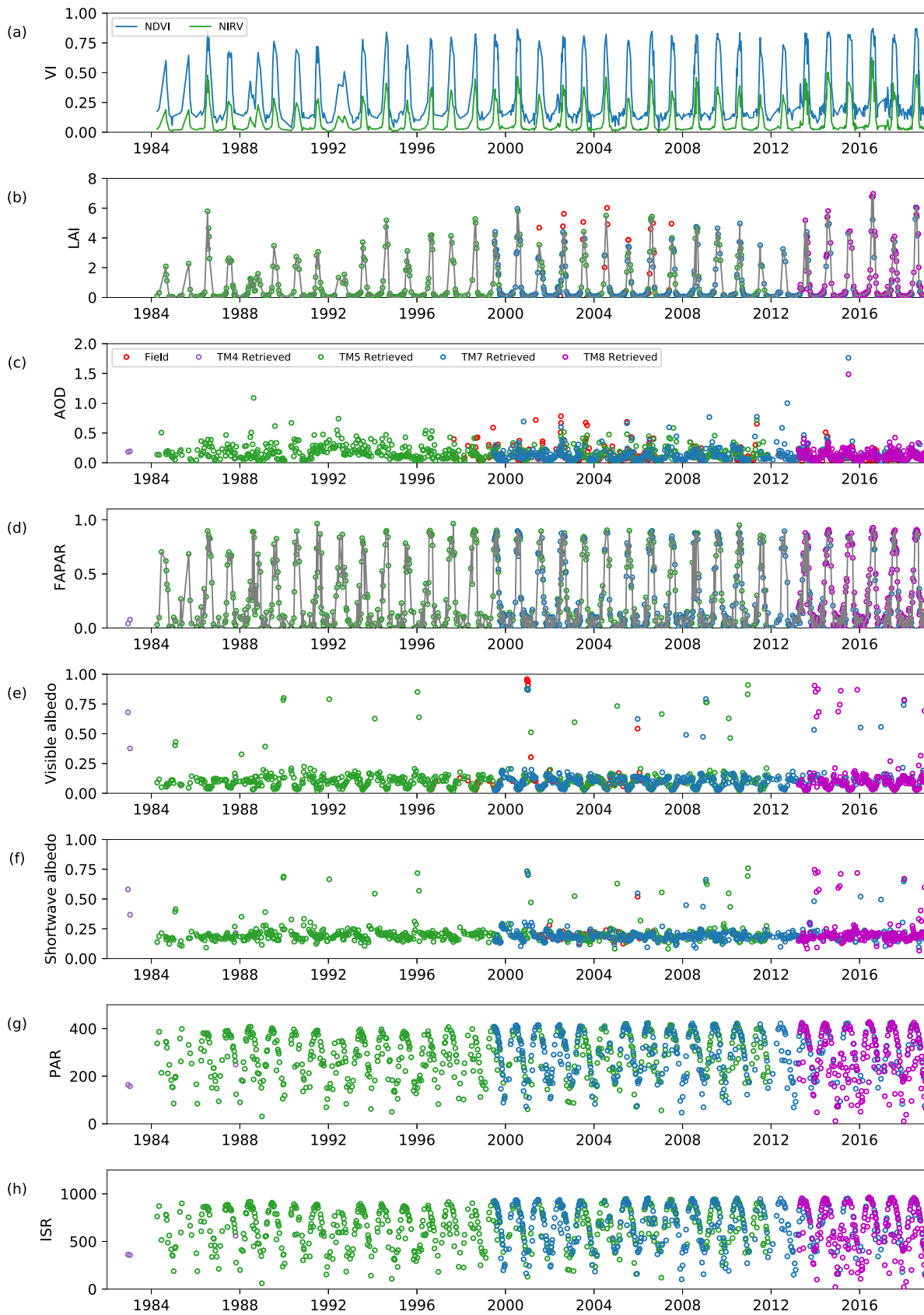


Fig. 7. Retrieved (b) LAI, (c) AOD at 550 nm, (d) FAPAR, (e) visible albedo, (f) shortwave albedo, (g) PAR, in W/m², and (h) ISR, in W/m² at the US-Bo1/AmeriFlux site, the corresponding NDVI and NIRV are also plotted in (a). For interpretation of the references to color in this figure legend, the reader is referred to the web version of this article.

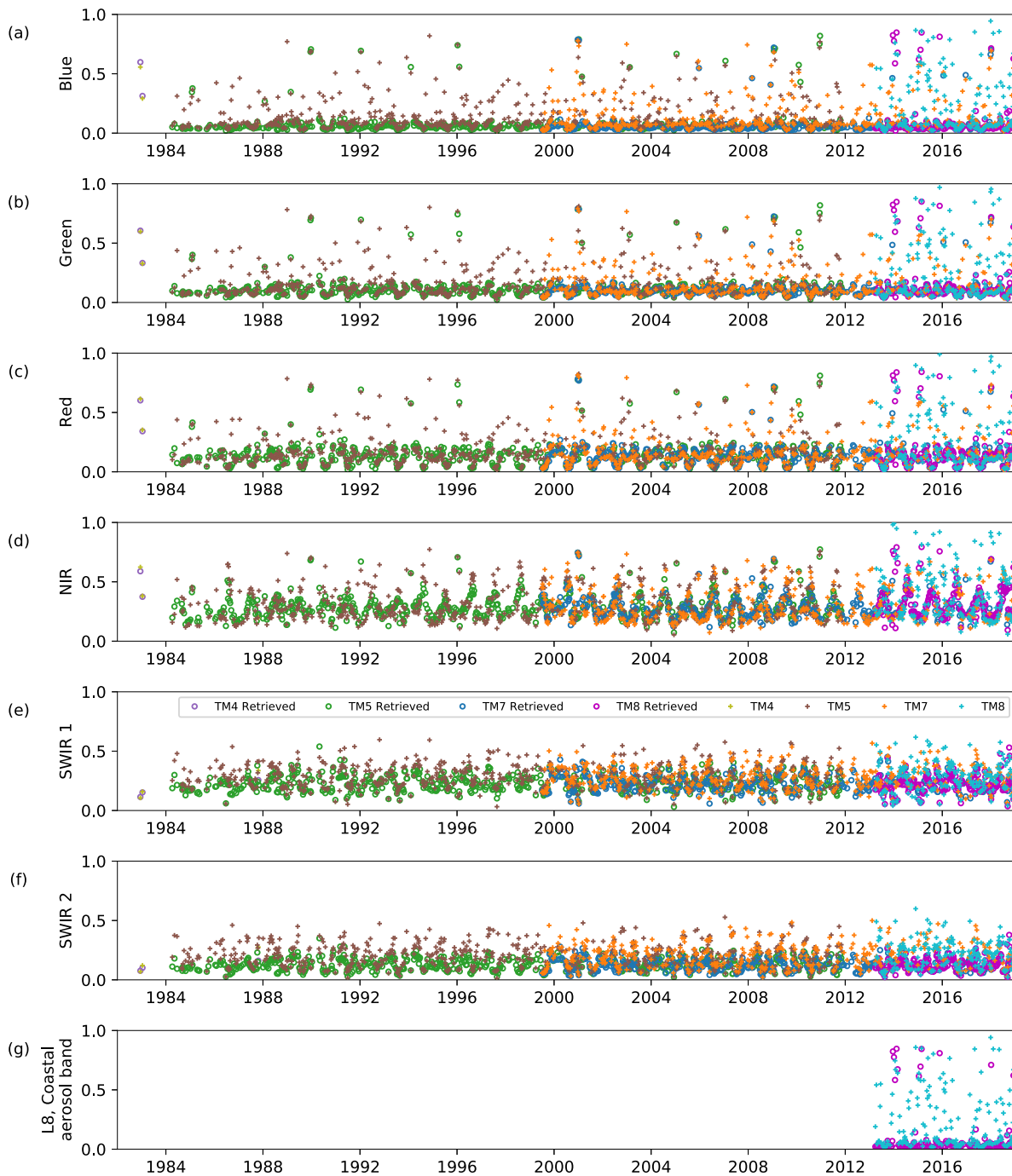


Fig. 8. Comparison of retrieved and Landsat 4–8 surface reflectance at the US-Bo1/AmeriFlux site. Only Landsat 8 has the Coastal aerosol band, which is plotted in (g). For interpretation of the references to color in this figure legend, the reader is referred to the web version of this article.

B. Landsat Data

The two-step parameter estimation algorithm was conducted over the 57 selected sites listed in Table III from corresponding long-term Landsat observations.

The retrieved results for US-Bo1/AmeriFlux are shown in Figs. 7 and 8. The 35-year estimated multiple parameters show reasonable seasonal trends. Only the results under clear-sky conditions are shown for the LAI and AOD. The normalized difference vegetation index (NDVI) [67] and the near-infrared reflectance of vegetation (NIRV) [68] from

the Landsat observations under clear-sky conditions are also given. However, it can be seen from Fig. 7(a) that there are still some jump values in the vegetation index (VI) curves (years 1986, 1989, 1992, 2002, 2008, 2010, 2013, 2016, and 2017), indicating imperfect cloud detection [69], [70]. The incorrect detection of clouds directly influences the retrieval results, such as jumps in the LAI and FAPAR at the corresponding times, as shown in Fig. 7(b) and (d), respectively. The retrieved albedo values have good fits against the field measurements, and the seasonal patterns are captured. Comparisons between the retrieved and Landsat sur-

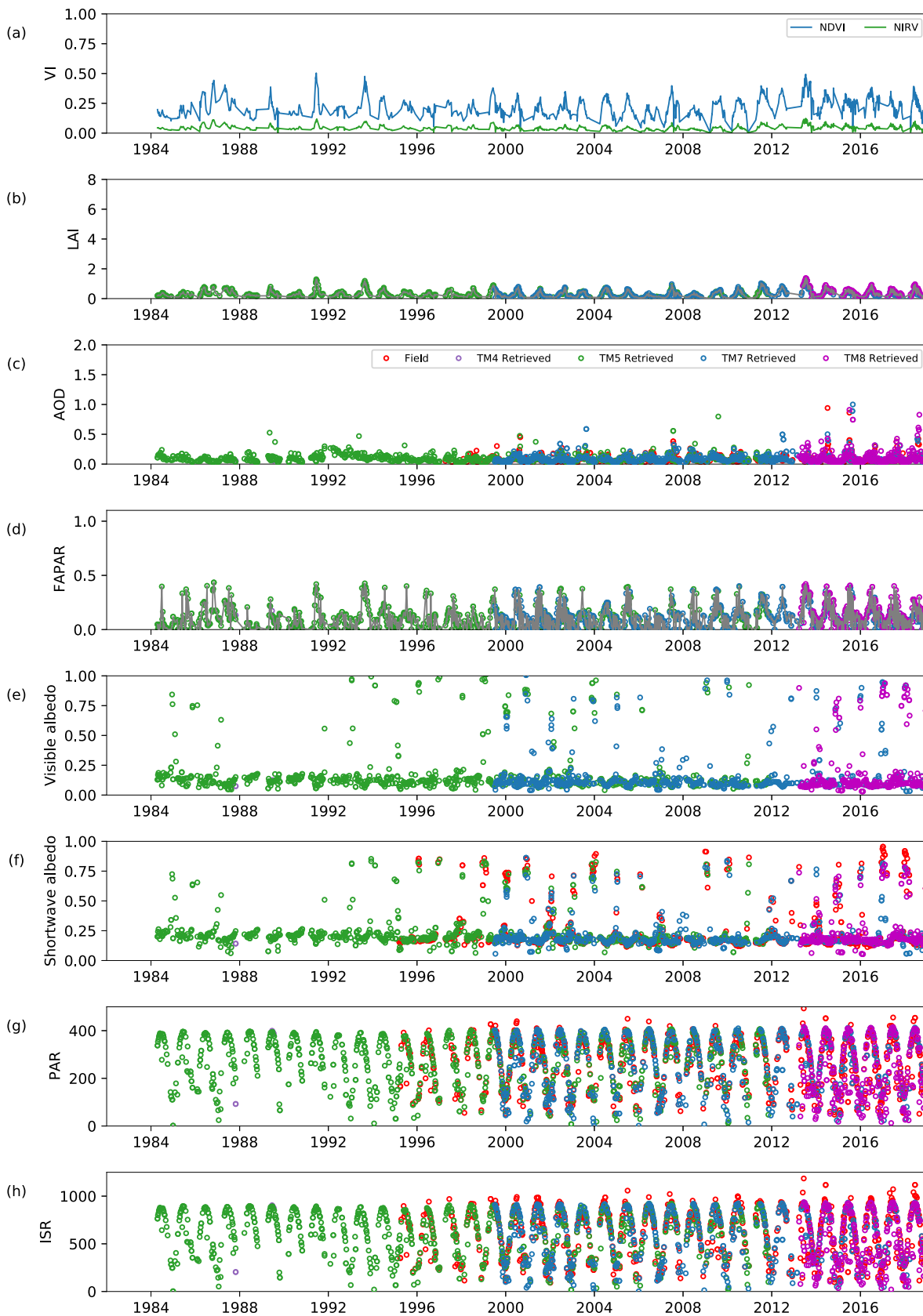


Fig. 9. Retrieved (b) LAI, (c) AOD at 550 nm, (d) FAPAR, (e) visible albedo, (f) shortwave albedo, (g) PAR, in W/m^2 , and (h) ISR, in W/m^2 at the FPK/SURFRAD site, the corresponding NDVI and NIRV are also plotted in (a). For interpretation of the references to color in this figure legend, the reader is referred to the web version of this article.

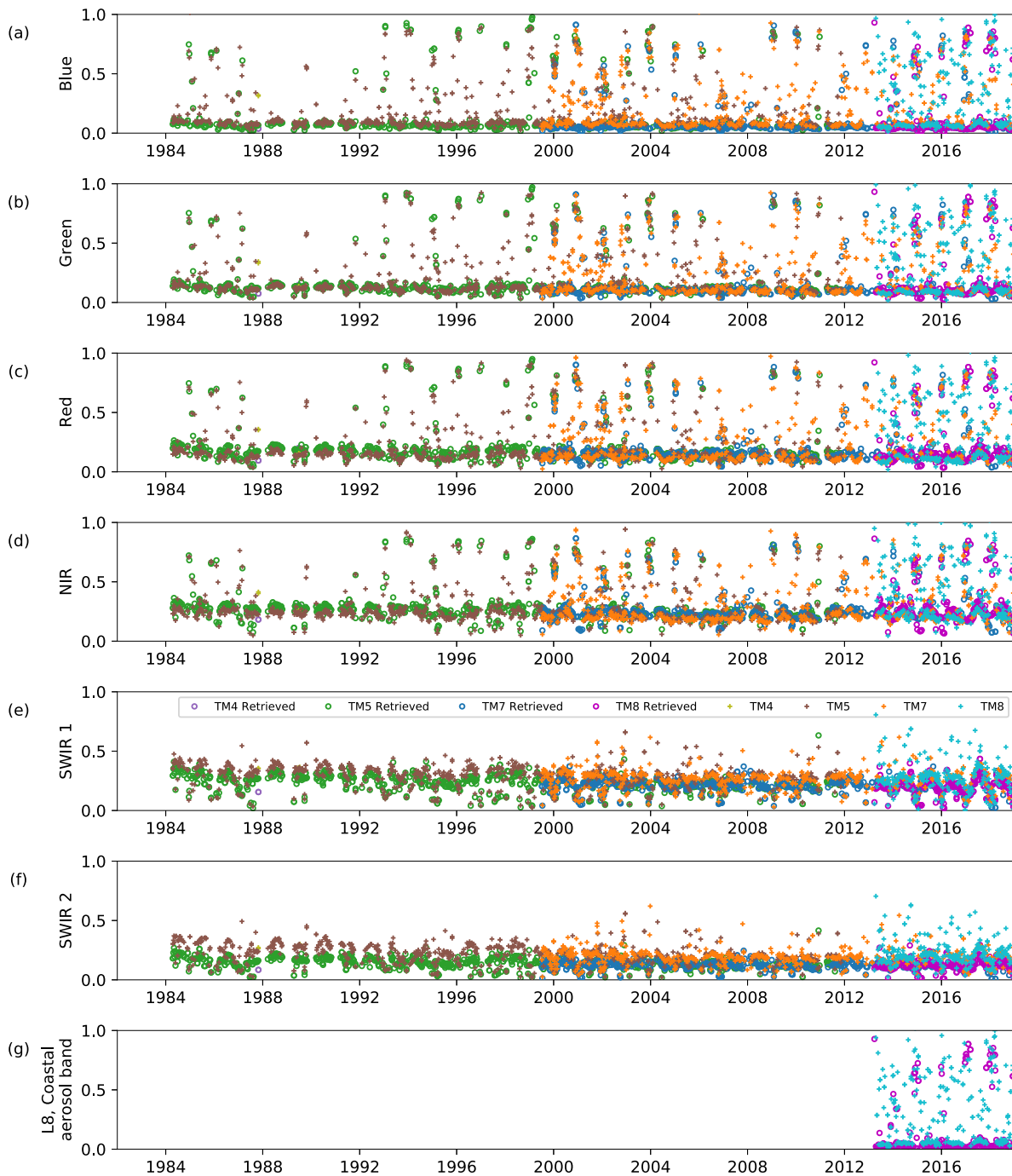


Fig. 10. Comparison of retrieved and Landsat 4–8 surface reflectance at the FPK/SURFRAD site. Only Landsat 8 has the Coastal aerosol band, which is plotted in (g). For interpretation of the references to color in this figure legend, the reader is referred to the web version of this article.

face reflectance values are shown in Fig. 8. The estimated values are plotted with circles, while the Landsat Level-2 surface reflectance product is plotted with plus signs. Significant numbers of high Landsat surface reflectance values are affected by clouds because the current Landsat atmospheric correction algorithm does not incorporate clouds [71], [72], while the estimated scheme provides reasonable values.

The retrieved results for FPK/SURFRAD are shown in Figs. 9 and 10. Although the LAI values are small at this

site, the seasonal patterns can be clearly identified, and slight jumps in the VI, LAI, and FAPAR curves can still be observed, such as in 1999 and 2007. The retrieved AOD shows a good fit with the field AOD values, as shown in Fig. 9(c). The retrieved shortwave albedo values are in good agreement with the field albedo and captured snow events. The retrieved PAR and ISR are given in the panels of Fig. 9(g) and (h), respectively. It can be seen that the estimated values match the field values on the seasonal changes and amplitudes well. However, there are a few spikes in the field ISR and PAR, such as in 2013,

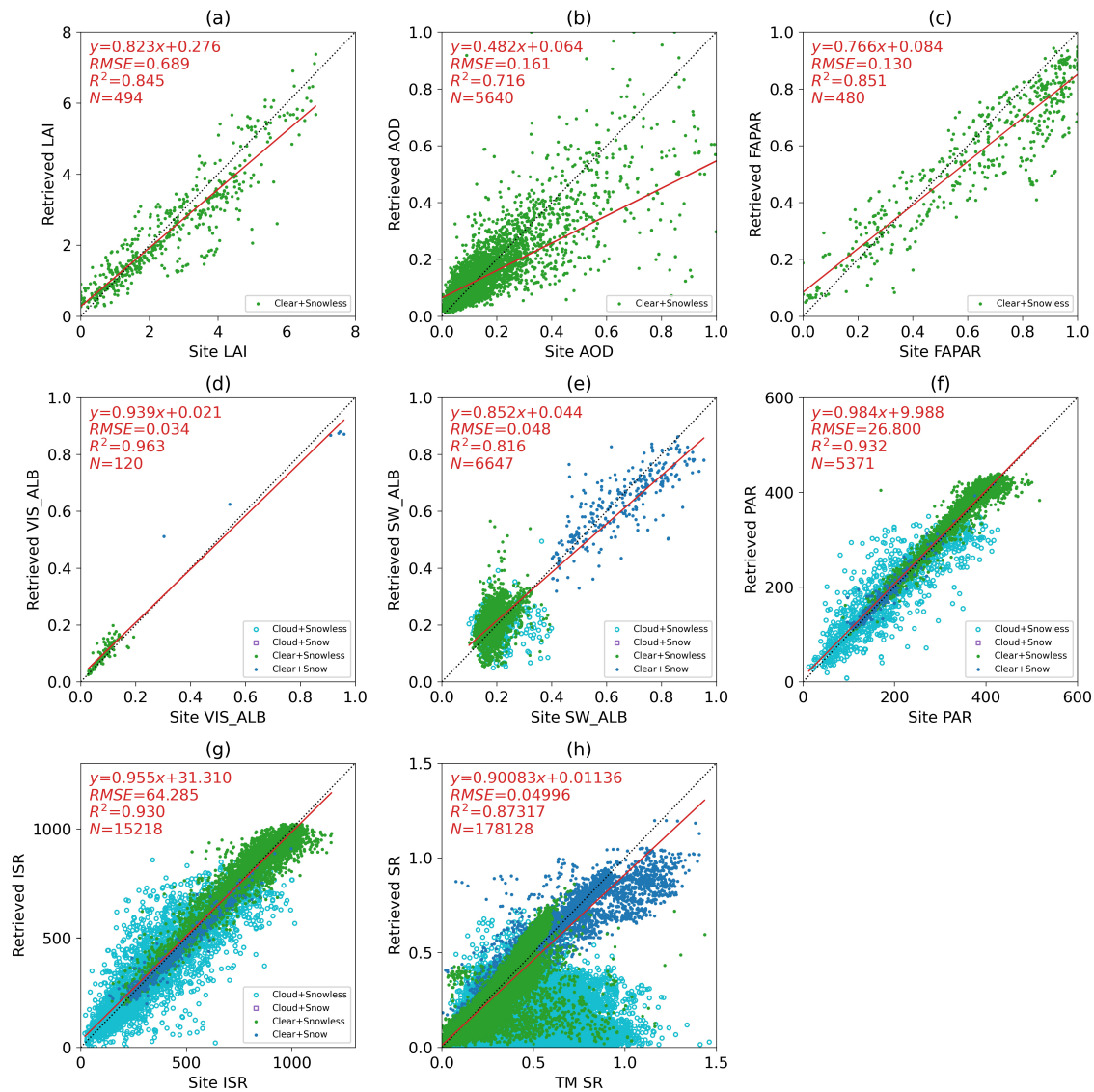


Fig. 11. Quantitative comparison of the estimated parameters with the field measurements over the selected site (a) LAI, (b) AOD at 550 nm, (c) FAPAR, (d) visible albedo, (e) shortwave albedo, (f) PAR, in W/m^2 , (g) ISR, in W/m^2 , and (h) comparison of the estimated surface reflectance with the Landsat Level-2 surface reflectance product. For interpretation of the references to color in this figure legend, the reader is referred to the web version of this article.

which might be attributed to errors in the field measurements. The comparison of the surface reflectances is shown in Fig. 10. The estimated values are generally consistent with the Landsat Level-2 surface reflectance product under clear-sky conditions, but the retrieved reflectance underestimates the Landsat product at the shortwave infrared (SWIR) bands. This underestimation when the LAI is very small might be caused by the applicability of the soil reflectance model, which is empirical and needs to be updated in the future [42], [73]. Similarly, it can be seen that the Landsat product is influenced by clouds and shows high reflectance values, while the estimated scheme can give reasonable results.

Only two sites with long-term results are shown to avoid repetitive and uninteresting descriptions. The overall scatter plots for all the sites are illustrated in Fig. 11. Direct comparisons of the retrieved LAI and FAPAR are

shown in Fig. 11(a) and (c), respectively. The field values of the LAI and FAPAR are primarily from the ImagineS and VALERI projects. The retrieved LAI and FAPAR are generally consistent with the field-measured values, where $RMSE_{LAI} = 0.69$ and $RMSE_{FAPAR} = 0.13$. However, the retrieved LAI and FAPAR values tend to underestimate the field measurements slightly in high-value regions. Evaluations of the retrieved visible and shortwave albedo values are shown in Fig. 11(d) and (e), respectively, and most of the estimated albedo values are near the 1:1 line. Evaluations of the PAR and ISR are shown in Fig. 11(f) and (g), respectively, and the estimation scheme performs well in general. However, as Shi *et al.* [74] discussed, an issue arises when evaluating the PAR and ISR. Taking the SURFRAD sites as an example, the field-measured radiation parameters are the 3-min or 1-min averaged values. The temporal resolution is very good,

but atmospheric conditions can change faster. The satellite observations are instantaneous, and it is possible that there are no clouds during the observation period, but clouds may arrive later and cause a decrease in the average radiation values. The comparison of the retrieved and Landsat Level-2 surface reflectance is shown in Fig. 11(h). The retrieved and Landsat surface reflectance fit well under clear conditions, while the main differences happen under cloudy conditions because the Landsat surface reflectance product gives large values under cloudy conditions, as shown in Fig. 11(h).

IV. DISCUSSION

Although the evaluation results demonstrate that the proposed parameter estimation scheme is accurate, several issues still need to be addressed or should be considered to improve the model in the future.

A. Phase Identification

Incorrect identification of atmospheric and surface conditions is the greatest challenge in this study. Landsat internal QC information was used in this study. Most of the QC information has very good accuracy, but some information still includes errors. As shown in Section III-B, incorrect identification of conditions can cause mistakes. The majority of misjudgements are with snow and clouds, both of which have high-reflectivity properties in the visible and near-infrared domains. In particular, it is very difficult to detect surface conditions if clouds, especially thick clouds, exist in the shortwave range because clouds are highly reflective from 400 to 2500 nm. A potential solution is the combination of passive microwave and/or synthetic aperture radar (SAR) remote sensing data, which will be considered in our future studies.

In addition, the LAI is currently filled with prior values under cloudy observations, which is not ideal. Unlike MODIS observations with a one-day visit frequency, the revisit time of Landsat is 16 days, which implies that using nearby clear observations as a replacement is impractical. Fusing with observations from other sensors, such as Sentinel-2, is a possible solution. Fusing with SAR observations is also a potential method, and an interesting study by Pipia *et al.* [75] gave promising results.

B. 3-D Effect of Clouds

The proposed surface-atmosphere model is a 1-D model, and it cannot handle the 3-D effect of clouds [13], [76]. This is another source of errors in the parameter estimation scheme. Although the atmosphere layer can be “replaced” by 3-D atmospheric radiative transfer models, from which the 3-D effect of clouds is incorporated, it would make the model too complex to be used in retrieval. Therefore, this 1-D model is used in the current estimation scheme.

C. Efficiency

Efficiency is another issue. Landsat data have wide spectral responses, as shown in Fig. 3, which require many computations for simulating TOA observations because convolutions

over the spectrum are needed. Also, the integration over the spectrum for radiation-related parameters is also time-consuming. Therefore, the current multiple parameter estimation algorithm is only suitable for processing small sites and is hard to apply for regional or global usage because it is computationally expensive.

Fortunately, recent developments in machine-learning techniques provide potential solutions to the efficiency issue. The first potential solution is using emulators to replace complex radiative transfer models [77], [78]. We have tested this method over flat surfaces in Shi *et al.* [74]. It did accelerate the estimation processes because the integration and convolution over the spectrum are avoided. However, iterations over the input parameter space to find optimal values are still needed because the optimization retrieval strategy is involved. The second potential solution is estimating parameters from TOA observations directly by training relationships between TOA observations and target parameters. A typical example can be found in Estévez *et al.* [23]. However, much more effort is needed when introducing the second method into the estimation scheme because multiple parameters are involved, and further tests are required, especially over rugged areas.

V. CONCLUSION

A two-step multiparameter estimation scheme is proposed to estimate the LAI, AOD, surface reflectance, albedo, FAPAR, PAR, and ISR from Landsat TOA observations. The coupled surface-atmosphere model incorporates atmospheric, canopy, soil, and snow models, and the combined atmospheric and topographic effects are simultaneously modeled. The validation of the two-step estimation scheme over 57 selected sites demonstrates that this estimation scheme can be successfully used for high-spatial-resolution observations, with good accuracy. The RMSE values of the LAI, AOD, FAPAR, visible albedo, shortwave albedo, PAR, and ISR are 0.69, 0.16, 0.13, 0.034, 0.047, 26.80, and 64.28 W/m², respectively. The accuracy would be greatly improved if better identification of the atmospheric and surface conditions was provided.

By using this two-step estimation algorithm: 1) Atmospheric and topographic effects are simultaneously coupled and considered, thus avoiding the complex atmospheric and topographic corrections of satellite observations, and the anisotropic property of the surface is effectively accounted for. 2) All parameters are estimated from the same coupled surface-atmosphere model, which ensures the physical connections among them, and the estimated parameter values are physically consistent.

Future studies will focus on improving the identification of clouds and snow and incorporating machine learning acceleration techniques. In addition, the applicability of this algorithm will be tested on other high-spatial-resolution observations, such as those from Sentinel-2.

APPENDIX A

BASICS OF THE FOUR-STREAM THEORY

Four-stream theory [29], [79] is the basic frame to couple the surface and atmospheric radiative transfer models, and a

brief introduction to the necessary background information is given here. Imagine a medium layer above an underlying surface. The reflectance matrix at the top of this coupled scene R_s^* can be expressed as follows [29]:

$$R_s^* = \begin{bmatrix} r_{sd}^* & r_{dd}^* \\ r_{so}^* & r_{do}^* \end{bmatrix} = R_t + T_u(I - R_s R_b)^{-1} R_s T_d \quad (15)$$

where R_s is the reflectance matrix of the underlying surface, R_b is the reflectance matrix for the bottom of the medium layer, and R_t is the reflectance matrix for the top surface of the isolated medium layer. T_d and T_u are the transmittance matrices for the incoming and outgoing radiation (direct and diffuse), respectively, and I is the identity matrix

$$R_s = \begin{bmatrix} r_{sd} & r_{dd} \\ r_{so} & r_{do} \end{bmatrix}, \quad R_t = \begin{bmatrix} \rho_{sd} & \rho_{dd} \\ \rho_{so} & \rho_{do} \end{bmatrix}, \quad R_b = \begin{bmatrix} 0 & 0 \\ \rho_{dd}^b & 0 \end{bmatrix} \\ T_d = \begin{bmatrix} \tau_{ss} & 0 \\ \tau_{sd} & \tau_{dd} \end{bmatrix}, \quad T_u = \begin{bmatrix} \tau_{dd} & 0 \\ \tau_{do} & \tau_{oo} \end{bmatrix} \quad (16)$$

where r indicates the reflection above the underlying surface or the ensemble system, ρ is the inner reflection of the medium layer, and τ is the transmission through the medium layer. The subscript “s” represents the direct flux in the solar direction, the subscript “d” represents the hemispherical diffuse flux, the superscript “b” represents bottom of atmosphere, and the subscript “o” indicates the radiance (times π) in the direction of observation. Table IV gives detailed explanations of the matrix elements [79]. By applying (15) and (16), a multilayer model can be established.

ACKNOWLEDGMENT

The authors are grateful to United States Geological Survey (USGS) for providing Landsat data and NASA Global Modeling and Assimilation Office (GMAO) for providing MERRA-2 AOD product. They want to express our thanks to the SURFRAD project team, the BSRN project team, the ImagineS program team, and the VALERI project team for providing ground validation data. The authors acknowledge the following AmeriFlux sites for their data records: US-Bo1 and US-WCr.

REFERENCES

- [1] J. Yang *et al.*, “The role of satellite remote sensing in climate change studies,” *Nature Climate Change*, vol. 3, no. 10, pp. 875–883, Oct. 2013.
- [2] J. A. Benediktsson, J. Chanussot, and W. M. Moon, “Very high-resolution remote sensing: Challenges and opportunities,” *Proc. IEEE*, vol. 100, no. 6, pp. 1907–1910, Jun. 2012.
- [3] Z. Zhu *et al.*, “Benefits of the free and open landsat data policy,” *Remote Sens. Environ.*, vol. 224, pp. 382–385, Apr. 2019.
- [4] A. Mousivand, W. Verhoef, M. Menenti, and B. Gorte, “Modeling top of atmosphere radiance over heterogeneous non-lambertian rugged terrain,” *Remote Sens.*, vol. 7, no. 6, pp. 8019–8044, Jun. 2015.
- [5] C. B. Schaaf, X. Li, and A. H. Strahler, “Topographic effects on bidirectional and hemispherical reflectances calculated with a geometric-optical canopy model,” *IEEE Trans. Geosci. Remote Sens.*, vol. 32, no. 6, pp. 1186–1193, Nov. 1994.
- [6] G. Yin, A. Li, W. Zhao, H. Jin, J. Bian, and S. Wu, “Modeling canopy reflectance over sloping terrain based on path length correction,” *IEEE Trans. Geosci. Remote Sens.*, vol. 55, no. 8, pp. 4597–4609, Aug. 2017.
- [7] J. Wen *et al.*, “Characterizing land surface anisotropic reflectance over rugged terrain: A review of concepts and recent developments,” *Remote Sens.*, vol. 10, no. 3, p. 370, Feb. 2018.

TABLE IV
TRANSMITTANCE AND REFLECTANCE VARIABLES
FOR SOIL AND CANOPY

| | |
|------------------------|---|
| r_{so}, r_{so}^* | Bi-directional reflectance factor of soil and ensemble system |
| r_{sd}, r_{sd}^* | Directional-hemispherical reflectance of soil and ensemble system |
| r_{do}, r_{do}^* | Hemispherical-directional reflectance factor of soil and ensemble system |
| r_{dd}, r_{dd}^* | Bi-hemispherical reflectance of soil and ensemble system |
| ρ_{so} | Bi-directional reflectance of the isolated canopy |
| ρ_{sd} | Directional-hemispherical reflectance of the isolated canopy |
| ρ_{do} | Hemispherical-directional reflectance of the isolated canopy |
| ρ_{dd} | Bi-hemispherical reflectance of the isolated canopy |
| τ_{ss}, τ_{oo} | Direct transmittance of the isolated canopy in incident and observation direction |
| τ_{sd} | Directional-hemispherical transmittance of the isolated canopy in incident direction |
| τ_{do} | Hemispherical-directional transmittance of the isolated canopy in observation direction |
| τ_{dd} | Bi-hemispherical transmittance of the isolated canopy |
| τ_{ssoo} | Joint two-way directional transmittance of the isolated canopy |

- [8] S. Wu *et al.*, “Modeling discrete forest anisotropic reflectance over a sloped surface with an extended GOMS and SAIL model,” *IEEE Trans. Geosci. Remote Sens.*, vol. 57, no. 2, pp. 944–957, Feb. 2019.
- [9] F. Gemmell, “An investigation of terrain effects on the inversion of a forest reflectance model,” *Remote Sens. Environ.*, vol. 65, no. 2, pp. 155–169, Aug. 1998.
- [10] A. Gonsamo and J. M. Chen, “Improved LAI algorithm implementation to MODIS data by incorporating background, topography, and foliage clumping information,” *IEEE Trans. Geosci. Remote Sens.*, vol. 52, no. 2, pp. 1076–1088, Feb. 2014.
- [11] B. Gao, L. Jia, and M. Menenti, “An improved method for retrieving land surface albedo over rugged terrain,” *IEEE Geosci. Remote Sens. Lett.*, vol. 11, no. 2, pp. 554–558, Feb. 2014.
- [12] P. Zhao, W. Fan, Y. Liu, X. Mu, X. Xu, and J. Peng, “Study of the remote sensing model of FAPAR over rugged terrains,” *Remote Sens.*, vol. 8, no. 4, p. 309, Apr. 2016.
- [13] G. Huang *et al.*, “Estimating surface solar irradiance from satellites: Past, present, and future perspectives,” *Remote Sens. Environ.*, vol. 233, Nov. 2019, Art. no. 111371.
- [14] B. Cao *et al.*, “A review of Earth surface thermal radiation directionality observing and modeling: Historical development, current status and perspectives,” *Remote Sens. Environ.*, vol. 232, Oct. 2019, Art. no. 111304.
- [15] H. Shi, Z. Xiao, S. Liang, and X. Zhang, “Consistent estimation of multiple parameters from MODIS top of atmosphere reflectance data using a coupled soil-canopy-atmosphere radiative transfer model,” *Remote Sens. Environ.*, vol. 184, pp. 40–57, Oct. 2016.
- [16] Q. Liu *et al.*, “Preliminary evaluation of the long-term GLASS albedo product,” *Int. J. Digit. Earth*, vol. 6, pp. 69–95, Dec. 2013.
- [17] T. Faurtyot, “Vegetation water and dry matter contents estimated from top-of-the-atmosphere reflectance data: A simulation study,” *Remote Sens. Environ.*, vol. 61, no. 1, pp. 34–45, Jul. 1997.
- [18] C. Lavernet, F. Baret, L. Hascoët, S. Buis, and F.-X. Le Dimet, “Multitemporal-patch ensemble inversion of coupled surface-atmosphere radiative transfer models for land surface characterization,” *Remote Sens. Environ.*, vol. 112, no. 3, pp. 851–861, Mar. 2008.

- [19] V. C. E. Laurent, W. Verhoef, J. G. P. W. Clevers, and M. E. Schaepman, "Estimating forest variables from top-of-atmosphere radiance satellite measurements using coupled radiative transfer models," *Remote Sens. Environ.*, vol. 115, no. 4, pp. 1043–1052, Apr. 2011.
- [20] V. C. E. Laurent, W. Verhoef, J. G. P. W. Clevers, and M. E. Schaepman, "Inversion of a coupled canopy-atmosphere model using multi-angular top-of-atmosphere radiance data: A forest case study," *Remote Sens. Environ.*, vol. 115, no. 10, pp. 2603–2612, Oct. 2011.
- [21] V. C. E. Laurent, M. E. Schaepman, W. Verhoef, J. Weyermann, and R. O. Chávez, "Bayesian object-based estimation of LAI and chlorophyll from a simulated Sentinel-2 top-of-atmosphere radiance image," *Remote Sens. Environ.*, vol. 140, pp. 318–329, Jan. 2014.
- [22] J. Verrelst, J. Vicent, J. P. Rivera-Caicedo, M. Lumbierres, P. Morcillo-Pallarés, and J. Moreno, "Global sensitivity analysis of leaf-canopy-atmosphere RTMs: Implications for biophysical variables retrieval from top-of-atmosphere radiance data," *Remote Sens.*, vol. 11, no. 16, p. 1923, Aug. 2019.
- [23] J. Estévez *et al.*, "Gaussian processes retrieval of LAI from Sentinel-2 top-of-atmosphere radiance data," *ISPRS J. Photogramm. Remote Sens.*, vol. 167, pp. 289–304, Sep. 2020.
- [24] H. Shi, Z. Xiao, S. Liang, and H. Ma, "A method for consistent estimation of multiple land surface parameters from MODIS top-of-atmosphere time series data," *IEEE Trans. Geosci. Remote Sens.*, vol. 55, no. 9, pp. 5158–5173, Sep. 2017.
- [25] H. Ma, S. Liang, Z. Xiao, and H. Shi, "Simultaneous inversion of multiple land surface parameters from MODIS optical-thermal observations," *ISPRS J. Photogramm. Remote Sens.*, vol. 128, pp. 240–254, Jun. 2017.
- [26] A. Loew *et al.*, "Do we (need to) care about canopy radiation schemes in DGVMs? Caveats and potential impacts," *Biogeosciences*, vol. 11, no. 7, pp. 1873–1897, Apr. 2014.
- [27] M. Chernetskiy *et al.*, "Estimation of FAPAR over croplands using MISR data and the Earth observation land data assimilation system (EOLDA)," *Remote Sens.*, vol. 9, no. 7, p. 656, Jun. 2017.
- [28] H. Shi, Z. Xiao, J. Wen, and S. Wu, "An optical-thermal surface-atmosphere radiative transfer model coupling framework with topographic effects," *IEEE Trans. Geosci. Remote Sens.*, early access, Dec. 24, 2020, doi: 10.1109/TGRS.2020.3044061.
- [29] W. Verhoef, "Earth observation modeling based on layer scattering matrices," *Remote Sens. Environ.*, vol. 17, no. 2, pp. 165–178, Apr. 1985.
- [30] C. Emde *et al.*, "The libRadtran software package for radiative transfer calculations (version 2.0.1)," *Geosci. Model Devices*, vol. 9, no. 5, pp. 1647–1672, May 2016.
- [31] S. Platnick *et al.*, "The MODIS cloud optical and microphysical products: Collection 6 updates and examples from Terra and Aqua," *IEEE Trans. Geosci. Remote Sens.*, vol. 55, no. 1, pp. 502–525, Jan. 2017.
- [32] M. Main-Knorn, B. Pflug, J. Louis, V. Debaecker, U. Müller-Wilm, and F. Gascon, "Sen2Cor for Sentinel-2," in *Image and Signal Processing for Remote Sensing XXIII*, vol. 10427. Warsaw, Poland: International Society for Optics and Photonics, Oct. 2017, Art. no. 1042704.
- [33] K. N. Liou, *An Introduction to Atmospheric Radiation* (International Geophysics), 2nd ed. Amsterdam, The Netherlands: Academic, May 2002.
- [34] A. A. Kokhanovsky and F.-M. Breon, "Validation of an analytical snow BRDF model using PARASOL multi-angular and multispectral observations," *IEEE Geosci. Remote Sens. Lett.*, vol. 9, no. 5, pp. 928–932, Sep. 2012.
- [35] S. G. Warren, "Optical constants of ice from the ultraviolet to the microwave," *Appl. Opt.*, vol. 23, no. 8, p. 1206, Apr. 1984.
- [36] A. A. Kokhanovsky, T. Aoki, A. Hachikubo, M. Hori, and E. P. Zege, "Reflective properties of natural snow: Approximate asymptotic theory versus *in situ* measurements," *IEEE Trans. Geosci. Remote Sens.*, vol. 43, no. 7, pp. 1529–1535, Jul. 2005.
- [37] A. Kuusk, "A multispectral canopy reflectance model," *Remote Sens. Environ.*, vol. 50, no. 2, pp. 75–82, Nov. 1994.
- [38] A. Kuusk, "A Markov chain model of canopy reflectance," *Agricult. Forest Meteorol.*, vol. 76, nos. 3–4, pp. 221–236, Oct. 1995.
- [39] A. Kuusk, "A two-layer canopy reflectance model," *J. Quant. Spectrosc. Radiat. Transf.*, vol. 71, no. 1, pp. 1–9, Oct. 2001.
- [40] J.-B. Féret, A. A. Gitelson, S. D. Noble, and S. Jacquemoud, "PROSPECT-D: Towards modeling leaf optical properties through a complete lifecycle," *Remote Sens. Environ.*, vol. 193, pp. 204–215, May 2017.
- [41] A. Kuusk, "Two-layer canopy reflectance model ACRM user guide Version 12.2012," Group Vegetation Remote Sens., Tartu Observatory, Tartu, Estonia, Tech. Rep., Dec. 2012.
- [42] C. L. Walthall, J. M. Norman, J. M. Welles, G. Campbell, and B. L. Blad, "Simple equation to approximate the bidirectional reflectance from vegetative canopies and bare soil surfaces," *Appl. Opt.*, vol. 24, no. 3, pp. 383–387, Feb. 1985.
- [43] T. Nilson and A. Kuusk, "A reflectance model for the homogeneous plant canopy and its inversion," *Remote Sens. Environ.*, vol. 27, no. 2, pp. 157–167, Feb. 1989.
- [44] J. C. Price, "On the information content of soil reflectance spectra," *Remote Sens. Environ.*, vol. 33, no. 2, pp. 113–121, Aug. 1990.
- [45] J. Dozier, J. Bruno, and P. Downey, "A faster solution to the horizon problem," *Comput. Geosci.*, vol. 7, no. 2, pp. 145–151, Jan. 1981.
- [46] J. Dozier and J. Frew, "Rapid calculation of terrain parameters for radiation modeling from digital elevation data," *IEEE Trans. Geosci. Remote Sens.*, vol. 28, no. 5, pp. 963–969, Sep. 1990.
- [47] A. Saltelli, "Making best use of model evaluations to compute sensitivity indices," *Comput. Phys. Commun.*, vol. 145, no. 2, pp. 280–297, May 2002.
- [48] A. Saltelli, P. Annoni, I. Azzini, F. Campolongo, M. Ratto, and S. Tarantola, "Variance based sensitivity analysis of model output. Design and estimator for the total sensitivity index," *Comput. Phys. Commun.*, vol. 181, no. 2, pp. 259–270, Feb. 2010.
- [49] A. Mousivand, M. Menenti, B. Gorte, and W. Verhoef, "Global sensitivity analysis of the spectral radiance of a soil-vegetation system," *Remote Sens. Environ.*, vol. 145, pp. 131–144, Apr. 2014.
- [50] J. Verrelst, J. P. Rivera, C. van der Tol, F. Magnani, G. Mohammed, and J. Moreno, "Global sensitivity analysis of the SCOPE model: What drives simulated canopy-leaving Sun-induced fluorescence?" *Remote Sens. Environ.*, vol. 166, pp. 8–21, Sep. 2015.
- [51] E. Priekaziuk and C. van der Tol, "Global sensitivity analysis of the SCOPE model in Sentinel-3 bands: Thermal domain focus," *Remote Sens.*, vol. 11, no. 20, p. 2424, Jan. 2019.
- [52] V. C. E. Laurent, W. Verhoef, A. Damm, M. E. Schaepman, and J. G. P. W. Clevers, "A Bayesian object-based approach for estimating vegetation biophysical and biochemical variables from APEX at-sensor radiance data," *Remote Sens. Environ.*, vol. 139, pp. 6–17, Dec. 2013.
- [53] Q. Y. Duan, V. K. Gupta, and S. Sorooshian, "Shuffled complex evolution approach for effective and efficient global minimization," *J. Optim. Theory Appl.*, vol. 76, no. 3, pp. 501–521, Mar. 1993.
- [54] J. Wu and X. Zhu, "Using the shuffled complex evolution global optimization method to solve groundwater management models," in *Frontiers of WWW Research and Development-APWeb*, X. Zhou, J. Li, H. T. Shen, M. Kitsuregawa, and Y. Zhang, Eds. Berlin, Germany: Springer, Jan. 2006, pp. 986–995.
- [55] Q. Duan, S. Sorooshian, and V. Gupta, "Effective and efficient global optimization for conceptual rainfall-runoff models," *Water Resour. Res.*, vol. 28, no. 4, pp. 1015–1031, Apr. 1992.
- [56] S. Foga *et al.*, "Cloud detection algorithm comparison and validation for operational landsat data products," *Remote Sens. Environ.*, vol. 194, pp. 379–390, Jun. 2017.
- [57] H. Fujisada, M. Urai, and A. Iwasaki, "Technical methodology for ASTER global DEM," *IEEE Trans. Geosci. Remote Sens.*, vol. 50, no. 10, pp. 3725–3736, Oct. 2012.
- [58] B. K. P. Horn, "Hill shading and the reflectance map," *Proc. IEEE*, vol. 69, no. 1, pp. 14–47, Jan. 1981.
- [59] Z. Xiao, S. Liang, J. Wang, Y. Xiang, X. Zhao, and J. Song, "Long-time-series global land surface satellite leaf area index product derived from MODIS and AVHRR surface reflectance," *IEEE Trans. Geosci. Remote Sens.*, vol. 54, no. 9, pp. 5301–5318, Sep. 2016.
- [60] C. A. Randles *et al.*, "The MERRA-2 aerosol reanalysis, 1980 onward. Part I: System description and data assimilation evaluation," *J. Climate*, vol. 30, no. 17, pp. 6823–6850, Apr. 2017.
- [61] V. Buchard *et al.*, "The MERRA-2 aerosol reanalysis, 1980 onward. Part II: Evaluation and case studies," *J. Climate*, vol. 30, no. 17, pp. 6851–6872, Jun. 2017.
- [62] H. Shi, Z. Xiao, X. Zhan, H. Ma, and X. Tian, "Evaluation of MODIS and two reanalysis aerosol optical depth products over AERONET sites," *Atmos. Res.*, vol. 220, pp. 75–80, May 2019.
- [63] Z. Jiao *et al.*, "An algorithm for the retrieval of the clumping index (CI) from the MODIS BRDF product using an adjusted version of the kernel-driven BRDF model," *Remote Sens. Environ.*, vol. 209, pp. 594–611, May 2018.
- [64] A. Driemel *et al.*, "Baseline surface radiation network (BSRN): Structure and data description (1992–2017)," *Earth Syst. Sci. Data*, vol. 10, no. 3, pp. 1491–1501, Aug. 2018.

- [65] H. Schmithüsen, R. Koppe, R. Sieger, and G. König-Langlo, "BSRN toolbox V2.5—A tool to create quality checked output files from BSRN datasets and station-to-archive files," Alfred Wegener Inst., Helmholtz Centre Polar Marine Res., Bremerhaven, Pangaea, Germany, Tech. Rep., 2019, doi: <http://dx.doi.org/10.1594/PANGAEA.901332>.
- [66] B. N. Holben *et al.*, "An emerging ground-based aerosol climatology: Aerosol optical depth from AERONET," *J. Geophys. Res., Atmos.*, vol. 106, no. D11, pp. 12067–12097, Jun. 2001.
- [67] C. J. Tucker, "Red and photographic infrared linear combinations for monitoring vegetation," *Remote Sens. Environ.*, vol. 8, no. 2, pp. 127–150, May 1979.
- [68] G. Badgley, C. B. Field, and J. A. Berry, "Canopy near-infrared reflectance and terrestrial photosynthesis," *Sci. Adv.*, vol. 3, no. 3, Mar. 2017, Art. no. e1602244.
- [69] M. Feng *et al.*, "Global surface reflectance products from landsat: Assessment using coincident MODIS observations," *Remote Sens. Environ.*, vol. 134, pp. 276–293, Jul. 2013.
- [70] M. Claverie, E. F. Vermote, B. Franch, and J. G. Masek, "Evaluation of the Landsat-5 TM and Landsat-7 ETM+ surface reflectance products," *Remote Sens. Environ.*, vol. 169, pp. 390–403, Nov. 2015.
- [71] J. G. Masek *et al.*, "A landsat surface reflectance dataset for North America, 1990–2000," *IEEE Geosci. Remote Sens. Lett.*, vol. 3, no. 1, pp. 68–72, Jan. 2006.
- [72] E. Vermote, C. Justice, M. Claverie, and B. Franch, "Preliminary analysis of the performance of the Landsat 8/OLI land surface reflectance product," *Remote Sens. Environ.*, vol. 185, pp. 46–56, Nov. 2016.
- [73] C. Jiang and H. Fang, "GSV: A general model for hyperspectral soil reflectance simulation," *Int. J. Appl. Earth Observ. Geoinf.*, vol. 83, Nov. 2019, Art. no. 101932.
- [74] H. Shi, Z. Xiao, and X. Tian, "Exploration of machine learning techniques in emulating a coupled soil–canopy–atmosphere radiative transfer model for multi-parameter estimation from satellite observations," *IEEE Trans. Geosci. Remote Sens.*, vol. 57, no. 11, pp. 8522–8533, Nov. 2019.
- [75] L. Pipia, J. Muñoz-Mari, E. Amin, S. Belda, G. Camps-Valls, and J. Verrelst, "Fusing optical and SAR time series for LAI gap filling with multioutput Gaussian processes," *Remote Sens. Environ.*, vol. 235, Dec. 2019, Art. no. 111452.
- [76] K. Wyser, W. O'Hirok, C. Gautier, and C. Jones, "Remote sensing of surface solar irradiance with corrections for 3-D cloud effects," *Remote Sens. Environ.*, vol. 80, no. 2, pp. 272–284, May 2002.
- [77] J. Gómez-Dans, P. Lewis, and M. Disney, "Efficient emulation of radiative transfer codes using Gaussian processes and application to land surface parameter inferences," *Remote Sens.*, vol. 8, no. 2, p. 119, Feb. 2016.
- [78] J. Vicent *et al.*, "Emulation as an accurate alternative to interpolation in sampling radiative transfer codes," *IEEE J. Sel. Topics Appl. Earth Observ. Remote Sens.*, vol. 11, no. 12, pp. 4918–4931, Dec. 2018.
- [79] W. Verhoef and H. Bach, "Simulation of hyperspectral and directional radiance images using coupled biophysical and atmospheric radiative transfer models," *Remote Sens. Environ.*, vol. 87, no. 1, pp. 23–41, Sep. 2003.



Hanyu Shi (Student Member, IEEE) received the B.S. and M.S. degrees from Beijing Normal University, Beijing, China, in 2014 and 2017, respectively, where he is pursuing the Ph.D. degree.

His research interests include radiative transfer and estimation of surface variables.



Zhiqiang Xiao (Member, IEEE) received the Ph.D. degree in geophysical prospecting and information technology from Central South University, Changsha, China, in 2004.

From 2004 to 2006, he was a Postdoctoral Research Associate with Beijing Normal University, Beijing, China, where he is a Professor with the Faculty of Geographical Science. His research focuses on retrieval of land biophysical parameters from remotely sensed data, assimilating radiometric observations into dynamic models.



Qian Wang received the B.E. degree in geographic information system from the Beijing University of Civil Engineering and Architecture, Beijing, China, in 2014.

He is working with Beijing Normal University. His main research interests focus on global quantitative remote sensing product generation on high performance computing (HPC) platform.



Dongxing Wu received the M.S. degree from Henan University, Kaifeng, China, in 2018. He is pursuing the Ph.D. degree with Beijing Normal University, Beijing, China.

His research interests include climate change and global carbon cycle.